Earthquake-induced landslides monitoring and survey by means of InSAR

Tayeb SMAIL[1], Mohamed ABED[1], Ahmed MEBARKI[2,3], Milan Lazecky[4,5]

[1]Department of Civil Engineering, Saad Dahlab University, Blida City, Algeria

[2]Univ Gustave Eiffel, Univ Paris Est Creteil, CNRS, UMR 8208, MSME, 5 Bd Descartes, F-77454 Marne-la-Vallée, France

[3]Nanjing Tech University, 5 New Mofan Rd, Gulou, Nanjing, Jiangsu, Chine - Permanent Guest Professor within "High-Level Foreign Talents Programme" grant

[4]IT4Innovations, VSB-TU Ostrava, 17, Listopadu 15, 70833 Ostrava-Poruba, Czech Republic

[5]School of Earth and Environment, University of Leeds, Leeds LS2 9JT, UK

Correspondence to: SMAIL Tayeb (st_gc@univ-blida.dz) and Ahmed MEBARKI (ahmed.mebarki@univ-eiffel.fr)

Abstract. This study uses interferometric SAR techniques to identify and track earthquake-induced landslides as well as lands prone to landslides, by detecting deformations in areas struck by earthquakes. The pilot study area investigates the Mila region in Algeria, which suffered significant landslides and structural damages (earthquake: Mw5, 2020-08-07). DInSAR analysis shows normal interferograms with small fringes. The Coherence Change Detection (CCD) and DInSAR analysis were able to identify many landslides and ground deformations confirmed also by Sentinel-2 optical images and field inspection. The most important displacement (2.5 m), located in Kherba neighborhood, caused severe damages to dwellings. It is worth notice that CCD and DInSAR are very useful since they were also able to identify ground cracks surrounding a large zone (3.94 Km^2 area) in Grarem City whereas the Sentinel-2 optical images could not detect them. Although, displacement time-series analysis of 224 interferograms (04-2015 to 09-2020) performed using LiCSBAS did not detect any pre-event geotechnical precursors, the post-event analysis shows a 110 mm/y subsidence velocity in the back-hillside of Kherba.

1 Introduction

Although it is still challenging to predict exactly where and when natural hazards (earthquakes, landslides, floods, etc.) might occur, the capacity to monitor and survey the zones prone to important landslides as well as the capacity to identify and locate those impacted by earthquakes are key issues in risks mitigation, reduction, preparedness and adaptation. Actually, since earthquakes and landslides might occur in many places worldwide, they might cause a huge number of victims, important socio-economic, assets damages and losses. Their impact can be significantly reduced thanks to satellite imaging which allows prediction and early alerts of some landslide cases (Jacquemart and Tiampo, 2021; Mazzanti et al., 2012; Moretto et al., 2021).

It is then worth detecting or predicting critical ground changes at specific places, either after a geotechnical hazard occurs due to landslides and earthquakes mainly, or before it is suddenly triggered (Bakon et al., 2014; Galve et al., 2015). Such challenges can be tackled by regular image processing oriented landslides areas monitoring, in the aftermath of earthquakes, using SAR interferometric methods and optical images, for instance. Actually, since SAR (Synthetic Aperture Radar) is an active sensor system that uses microwave signals to collect data backscattered from the earth's surface, the use of satellite imaging systems like Interferometric SAR methods appears as a cost-effective way for measuring millimeter-level displacements of the earth surface (Herrera et al., 2009), at a regional scale and can be used as an early warning system for the safety of structures and their surroundings (Galve et al., 2015; Roque et al., 2015).

The expected outcomes are based upon the processing of SAR data as it uses Differential InSAR (DInSAR), Coherence Change Detection (CCD), and time series analysis (LiCSBAS software). LiCSBAS exploits the LiCSAR data that process InSAR datasets automatically (Sentinel-1), taking advantage of high-resolution SAR sensing, in order to track ground changes and landslides.

The SAR analyses aim to detect ground deformations through DInSAR and CCD investigations as they consider, for illustrative purposes, a city in Algeria struck by an earthquake (August 7, 2020: Algeria, Mila): the ground deformations and displacements, in Kherba City and Grarem City (northeastern part of Mila downtown, 2 km) are investigated. The affected areas span over 3.94 km^2 for Grarem and 2.1 km^2 for the Kherba landslides. Furthermore, a time-series analysis of LiCSAR data performed out by LiCSBAS software, investigates the possible existence of precursors in geotechnical conditions.

2 Land and ground movements monitoring and surveying in the aftermath of an earthquake

2.1 Satellite images and methods - Case study

The present research study is multifold. It aims to use InSAR image processing for various purposes, in the case of landslides and earthquakes:

- Use the InSAR in the aftermath of an earthquake in order to identify the geotechnical displacements or deformations, their extent, and locations. The Differential radar interferometry and the Coherence Changes Detection are the most adapted methods for ground and soil surfaces changes detection (Jung and Yun, 2020; Meng et al., 2020; Pawluszek-Filipiak and Borkowski, 2020; Tampuu et al., 2020; Tzouvaras et al., 2020). A city, Mila, in Northern Algeria, is considered as the pilot study. It has been struck by an earthquake in August 2020. The landslides and surface cracks have been affected significantly, during the earthquake events series, two distinct zones being distant by almost 15 km from each other (Kherba and Grarem).

- Use time-series analysis to investigate the displacements and their velocities before and after the occurrence of the main shock. For the city of Mila, the time series is performed out for a period extending from April 2015 up to October 2020, i.e. a long period before (*5 entire years*) the main shock in order to avoid a disturbance or bias that might be related to seasonal effects such as rains and vegetation effects (Lazeckỳ et al., 2020a), and a short period (*4 months*) ahead of the event date in order to investigate the historical development of the landslide.

- Compare and correlate the InSAR images processing results with the satellite optical images observations.

2.2 Pilot zone, earthquakes and landslides - Observed disorders

The case study area lies in Mila Province which is located in the northeast part of Algeria (Mediterranean zone), near the Dam of Beni Haroun. The Mediterranean zone is seismically active because of the northward convergence (4-10 mm/yr) of the African plate relative to the Eurasian plate along a complex plate boundary (Frizon de Lamotte et al., 2000; Mouloud and Badreddine, 2017; Peláez Montilla et al., 2003; USGS, n.d.). Throughout the last years, several landslide events have taken place in the wider region of Mila (Merghadi et al., 2018). Merghadi et al.(2018) constructed a detailed landslide inventory map of the study area. The seismic activities and landslides pose a persistent threat for built-up areas and facilities, such as roadways, bridges and tunnels, which need continuous monitoring and survey.

After an earthquake (Mw 5, 2020-08-07, epicenter 36.550° N - 6.271° E, Depth=10 km, (USGS)) that struck this region, important landslides were mostly observed in Mila City and its surroundings, see Figs. 1-3. Although, the earthquake was moderate, Beni Haroun Dam and the two large bridges built on the RN 27 highway needs to be inspected and their possible displacements monitored.

(a)   **(b)**
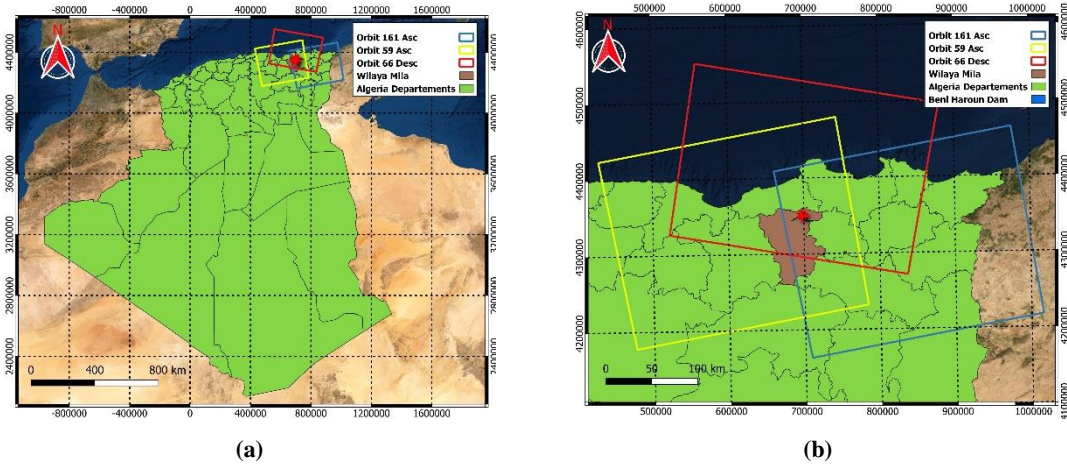
Figure 1. Mila location map (a), ascending and descending orbits footprints. Red stars indicate earthquake epicenter (QGIS, ESRI basemap).

In the present, two areas are studied, i.e. Kherba and Grarem Cities. The altitude at the top point 1 (Fig. 2.a) in Kherba hill is 654 m and 411 m for the upper point (2), located at 2.14 km distance with 11.34% slope. The maximum ground horizontal offset reached 2.5 m and the vertical deformations exceed 1.8 m (Fig. 3.b) at the top of Kherba hill (point A Fig. 2.a). The slope failure boundary of Kherba City is mapped as shown in Fig. 2.b. The Grarem area of interest (AoI) is located east north of Mila in hilly ground with an average slope reaching 12.5%, see Fig. 2.c.

(a)   **(b)**   **(c)**
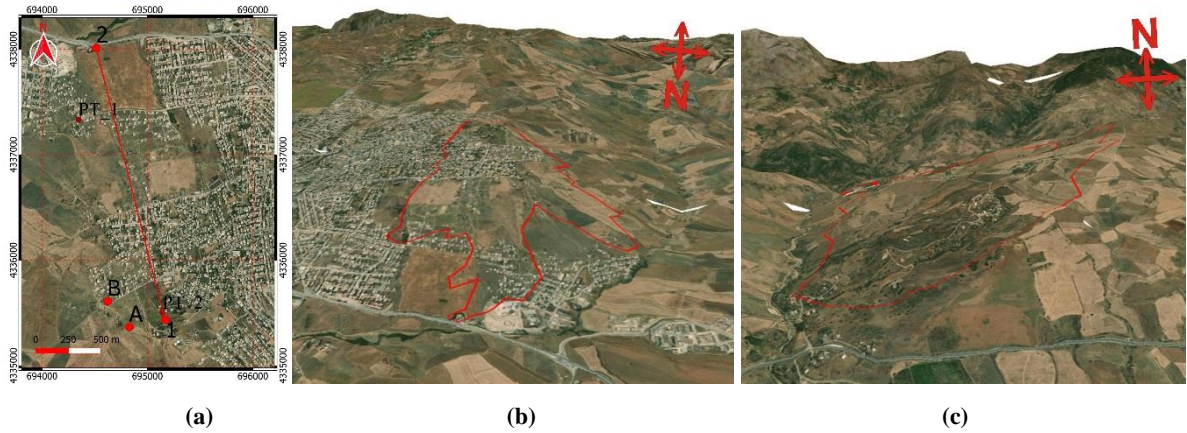
Figure 2. 3D view of AoIs, Kherba AoI and Grarem using QGIS with DEM SRTM 1sec and ESRI basemap, a & b are Kherba AoI, c is the Grarem case area, the red polygon is the boundary of change detected by InSAR.

(a)   **(b)**   **(c)**

Figure 3. Ground cracks due to landslides in Kherba, Mila, ~2.5m offset towards the North, a. Drone aerial photo from (LNHC), b. & c.- Lateral displacements (*Photos: courtesy M. Yacoub A., University of Setif, Algeria*).

2.3 Pilot zone - Data and images collection

The dataset used for this study is collected from European Space Agency (ESA), via the Copernicus Open Access portal, and from the Alaska Satellite Facility (ASF DAAC). The C-band Sentinel-1 A and B, launched in 2014 and 2016 respectively, provide regular datasets. The Sentinel-1 sensors have a wavelength of 5.546 cm (ESA), suitable for change detection and monitoring of large areas, and are right side-looking with an incidence angle ranging approximately from 20° to 46° (ESA,

2012). For the InSAR use, the Interferometric Wide (IW) swath Single Look Complex (SLC) data is selected and processed with the open-source software SNAP (Sentinel Applications Platform). It is worth using data from many orbits to monitor the AoIs due to different oriented directions, incidence angles of satellites, and the ground topography. The optical images of Sentinel-2 satellites are obtained from ESA, whereas downloading and processing data is done via QGIS, Semi-Automatic Classification Plugin (SCP) (Congedo, 2021).

For Mila region, the AoI is covered by 3 orbits, two are ascending (66, 59) and one is descending (161) (Fig. 1). Since the present study intends to detect the areas influenced by landslides, many pre-event and post-event data were used. Eighteen Sentinel-1 A and 17 Sentinel-1 B images (a total of 35) were downloaded to monitor Mila's area for the period from 1 July 2020 to 26 October 2020. Table 1 summarizes the appropriate interferograms, i.e. those having small perpendicular baselines and short temporal baselines. Tables 1, 2, and 2bis present all the images, their labels as IFG-ID, Orbits, and dates of acquisition.

Table 1. Characteristics of Sentinel-1 InSAR pairs used for this study.

IFG-ID	Track	M Date	S Date	Bp [m]	Bt [days]
IFG-0		2020-07-22	2020-07-28	-9.99	6
IFG-1		2020-07-28	2020-08-03	40.90	6
IFG-2		2020-07-28	2020-08-03	40.62	6
IFG-3		2020-08-03	2020-08-09	-51.47	6
IFG-4		2020-08-03	2020-08-09	-50.76	6
IFG-5		2020-08-09	2020-08-15	-27.57	6
IFG-6		2020-08-09	2020-08-15	27.62	6
IFG-7	**66 ASCENDING**	2020-08-15	2020-08-21	-16.19	6
IFG-8		2020-08-21	2020-08-27	42.43	6
IFG-9		2020-08-27	2020-09-02	-28.59	6
IFG-10		2020-09-02	2020-09-08	29.26	6
IFG-11		2020-09-08	2020-09-14	17.95	6
IFG-12		2020-09-14	2020-09-20	-6.05	6
IFG-13		2020-09-20	2020-10-02	-4.64	12
IFG-14		2020-10-02	2020-10-14	18.13	12
IFG-15		2020-10-14	2020-10-26	-49.36	12
IFG-16		2020-07-27	2020-08-02	69.64	6
IFG-17		2020-08-02	2020-08-08	-75.10	6
IFG-18	**59 ASCENDING**	2020-08-08	2020-08-14	-8.86	6
IFG-19		2020-08-14	2020-08-20	175.97	6
IFG-20		2020-08-20	2020-08-26	-226.75	6
IFG-21		2020-07-22	2020-07-28	-169.19	6
IFG-22		2020-07-28	2020-08-09	30.39	12
IFG-23		2020-07-28	2020-08-03	99.88	6
IFG-24	**161 DESCENDING**	2020-08-03	2020-08-09	-70.12	6
IFG-25		2020-08-09	2020-08-15	2.14	6
IFG-26		2020-08-15	2020-08-21	121.22	6
IFG-27		2020-08-21	2020-08-27	-196.82	6

Bt: temporal baseline; **Bp**: perpendicular baseline.

108   The temporal baselines for all InSAR pairs are 6 days, except the last three pairs of the ascending orbit 66 that have 12 days.

109   Furthermore, since a bad coherence map of the IFG-24 (Orbit 161), may lead to misinterpretation of results, prior acquisition

110   data (before the 3rd of August) is selected to generate the co-event interferogram (IFG-22). Therefore the temporal baseline is

111   12 days. The gray rows in Table 1 represent the co-event interferograms of the three orbits. The perpendicular baselines

112   guarantee also a good quality of InSAR studies (Braun, 2019). As LiCSBAS time series analysis aims to investigate long

113   period displacements and velocities over a large area: 34 interferograms from orbit 66 and 190 interferograms collected from

114   the 161 ascending track (Table 2), are selected for the present study.

115   **Table 2.** LiCSAR frames, analyzing periods and the total number of IFGs used in this study.

Frame ID	Date		Period	IFGs
	Start	End		
161A_05343_090806	2015-4-26	2020-9-26	66 month	190
066D_05394_131311	2020-4-5	2020-9-26	6 months	34

116   **Table 2bis.** Sentinel-2 optical images collected for the study case.

Frame ID	Date	Duration days, to the main shock
Image 1	2020-07-30	-7 days
Image 2	2020-08-09	+ 2 days

117   **3 Methodology description and results**

118   Four aspects are investigated and compared in the present case study:

119   - The SAR Interferometric (InSAR) methodology, which is subdivided into three sub-groups:

120   - DInSAR for the phase changes (fringes),

121   - CDD for the coherence change detection,

122   - Time series analysis and LiCSAR data.

123   - The optical image processing.

124   Every image contains the description of its source, i.e. IFG-ID (Tables 1, 2, and 2bis) or the image's acquisitions dates.

125   **3.1 SAR Interferometric methodology**

126   The Synthetic Aperture Radar (SAR) is an active microwave imaging system. It is independent of sunlight and penetrates

127   clouds, unlike passive optical imaging systems. The interferometric SAR method uses the phase components of co-registered

128   SAR images of the same pixel to estimate the topography and to measure the surface change in the target area (Kim, 2013).

129   At least two constellation images are needed to generate an interferogram, which contains topographic, atmospheric effect,

130   baseline error, and noise components (Goudarzi, 2010; Kim, 2013; Netzband et al., 2007):

131    $\phi = \phi_{disp} + \phi_{flat} + \phi_{topo} + \phi_{atm} + \phi_{orbit} + \phi_{noise}$ (1)

132   Where ϕ_{disp} is the line-of-sight (LOS) displacement, ϕ_{flat} the flat earth phase, ϕ_{topo} the topographic phase, ϕ_{atm} is an

133   atmospheric phase, ϕ_{orbit} , the baseline phase and ϕ_{noise} is noise phase contribution (Kim, 2013).

134   The main steps of processing data using SNAP software (DInSAR and CCD) are depicted in Fig. 4. It's worth notice that

135   for CCD processing, it is not necessary to follow the whole (DInSAR, Phase Unwrapping, and Phase to displacement).
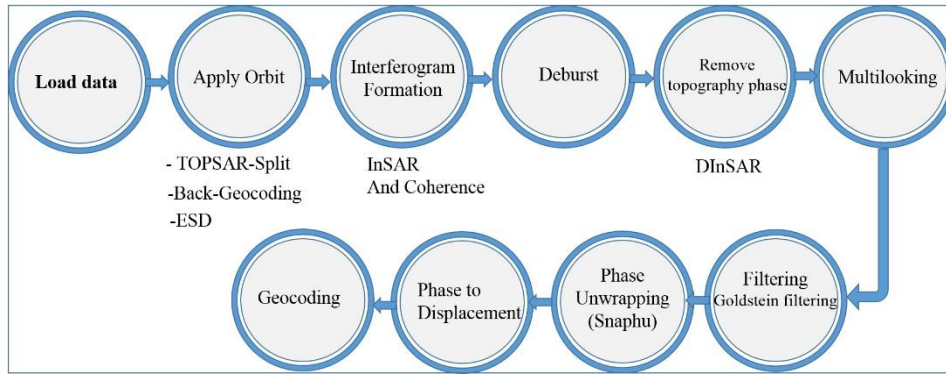
Figure 4. Workflow chart for the DInSAR processing using (SNAP) software.

3.1.1 Differential radar interferometry (DInSAR)

Differential radar interferometry (DInSAR) exploits the phase difference to measure coherent changes or deformation between two image acquisitions. It is often used for ground subsidence measurement (Canaslan Çomut et al., 2020; Galve et al., 2015). One of DInSAR's limitations is that the changes are not measurable in the case of non-coherent events (e.g., rapid landslide) (Braun, 2019) such as the present study.

3.1.2 Coherence Change Detection (CCD)

The estimated coherence is considered as a quality indicator of an interferogram (Jacquemart and Tiampo, 2021). Actually, it indicates that the phase and amplitude of the received signal express the degree of similarity between the images pair. The pixel coherence γ of two SAR images is estimated on the basis of N neighboring pixels (Jia et al., 2019; Wang et al., 2018).

$$\gamma = \frac{\sum_{i=1}^{N} S_{1i} S_{2i}^*}{\sqrt{\sum_{i=1}^{N} |S_{1i}|^2 \sum_{i=1}^{N} |S_{2i}|^2}} \tag{2}$$

Where: S_{1i}, S_{2i}, are the complex signal values of the SAR image pair, N is the window of neighboring pixels, $*$ is the complex conjugate.

The coherence values range between 0 and 1 so that the map is represented as a gray color which 0 is white and 1 is black.

3.1.3 Time series analysis and LiCSAR data

The "*Looking into Continents from Space with Synthetic Aperture Radar*" (LiCSAR) system processes automatically Sentinel-1 datasets for InSAR use, and generates wrapped, unwrapped interferograms and coherence maps (Lazeckỳ et al., 2020b), with a final product resolution of ~26.5 m (Lazeckỳ et al., 2020a). For such purposes, the open-source LiCSBAS software, adopted in the present study, is used for InSAR time series analysis based on LiCSAR data. It can generate maps of LOS displacement velocity and deformation time series for all processed frames. Furthermore, it is easy to implement and does not request high-performance computing facilities (Morishita, 2021).

In addition, the mechanism of landslides can be thoroughly studied through LiCSBAS analyses. They rely on the InSAR time-series analysis package integrated with LiCSAR, (Lazeckỳ et al., 2020b). Such time-series analyses are very useful in identifying, for a given landslide or ground deformations and displacements, the prior patterns of ground movements versus the time.

3.2 Optical image processing

The optical sensors are passive detection means that need sunlight and clear weather conditions to exploit the data. The Sentinel-2 is a multi-spectral instrument (MSI) that measures reflected solar radiance in 13 bands with a spatial moderate-resolution of 10 m in the red, green, blue, and near-infrared bands (Laneve et al., 2021).

166 The optical data collected from the ESA platform (Sentinel-2) is treated and plotted using QGIS software to generate true color
167 images (bands 2, 3, and 4 corresponding to RGB). The present study skips the image of 3rd, Aug 2020 due to bad weather
168 conditions, so that only the two images collected and mentioned in the table 2bis were used to validate the ground changes
169 detected by InSAR.

4 Application to the case study and results

171 The case studies are located in two different sites and both areas of interest are located in Algeria. They have a hilly relief: the
172 first one is located northeast of Mila City (Grarem) and the second is at the west part of Mila City (Kherba). To monitor the
173 AoIs, several images are processed and used with different orbits directions (total of 35 ascending and descending acquisitions,
174 see Fig. 1), to catch deformation from different angles along the sensor's LOS. The InSAR technique is used in both areas, to
175 detect land deformation and landslides triggered by the earthquake.

176 The adopted methods are applied for Mila case study to:
177   - detect and measure the co-event surface displacements and landslides, caused by the earthquake (CCD and DInSAR)
178   - monitor their dynamic evolution in the first weeks and months, at the post-event period (CCD and LiCSAR data).
179   - analyze their possible initiation ahead of the earthquake by months and years, at the pre-event period (Time-series
180   methods and LiCSAR data).
181   - corroborate the results by comparing several methods outputs, i.e. SAR (CCD, DInSAR, LiCSAR), aerial optical photo
182   (Sentinel-2), and field surveys.

183 The quality of the SAR image is consistent with the topography slopes and area roughness. Actually, the AoI has rough
184 topography, hills, and rivers (Fig. 2). Selecting either ascending or descending passes, relying on which will avoid some
185 limitation of InSAR is an extremely essential action to infer the deformation from various angles. Therefore, considering the
186 regional topography and geology of the AoI is necessary to process InSAR and results interpreting.

187 Differential InSAR (DInSAR) method is helpful to investigate co-seismic effects and detect ground changes. The produced
188 Interferograms and coherence images are projected to WGS84 reference, with a pixel size of 13.4 m. The unwrapped
189 interferograms present phase contribution of many noise resources (atmospheric), see Fig. 5. In general, strong earthquakes
190 cause large-scale fringes patterns around the epicenter which is not the case in the event under study (a moderate earthquake).
191 Processing DInSAR analysis may then lead to misinterpretation due to atmospheric contribution in differential phase
192 interferograms (Fig. 5). In the study case, no regional deformation due to the earthquake is observed and there is no need to
193 continue investigating the dam and the two bridges by simple DInSAR. However, to monitor the dam and bridges, it is highly
194 recommended to use PS-InSAR for regional and local ground deformation detection (Hooper et al., 2004; Rapant et al., 2020;
195 Sanabria et al., 2014).
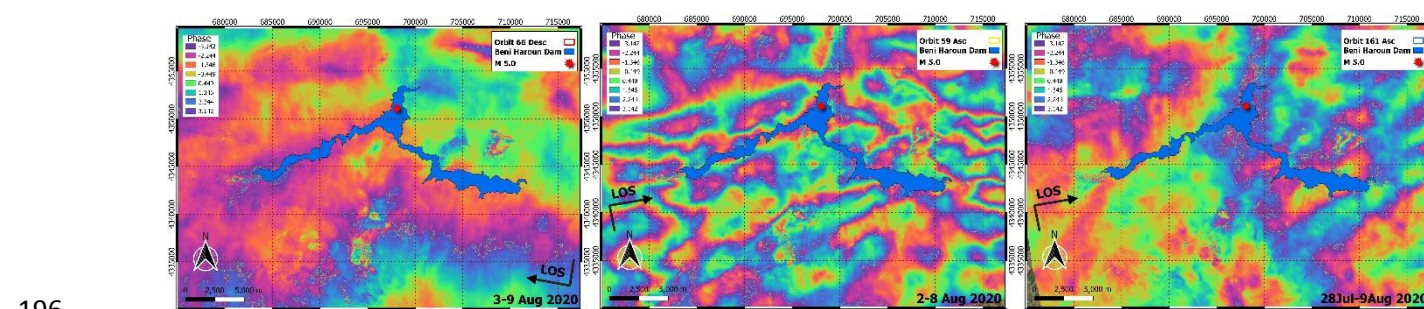
Figure 5. Wrapped Interferograms from Sentinel-1 for IFG-3+IFG-4, IFG-17 and IFG-22, The red star is the epicenter location (USGS).

`7
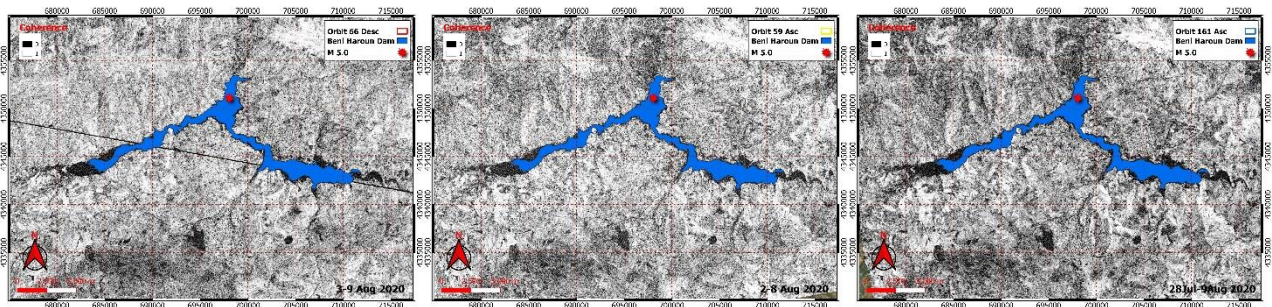
Figure 6. Mila Area, InSAR coherence maps for IFG-3+IFG-4, IFG-17 and IFG-22.

This moderate earthquake has triggered small deformation and landslides in Grarem, Kherba, and Azeba. The IFG-3 and IFG-4 are merged in one image due to the AoIs (Kherba and Grarem), which are located in two different image acquisitions of the descending orbit number 66.

4.1 Case of GRAREM

The detection of deformation or changes between two InSAR images reveals a small change in the region of Grarem. This change is observed as small fringes, each fringe corresponding to a displacement of a half-wavelength (λ=5.546 cm) in the LOS direction (Fig. 7). Usually, coherent change does not appear in coherence images as dark region, but in the study case, the outer borderline of the fringes region shows incoherence change which is clearly visible in coherence maps (Fig. 8).
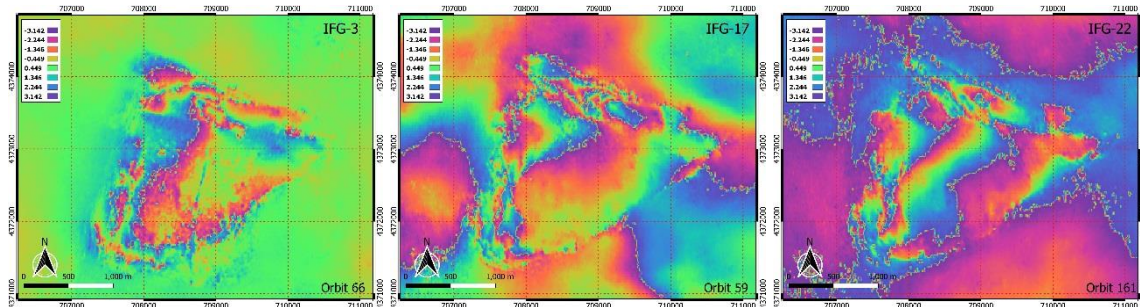
Figure 7. Detected fringes in Interferograms N° 3, 17, and 22, focused images on Grarem zone.

A time-series analysis needs then to be performed out to prove whether this contour was formed at the event occurrence date (August 7, 2020). The coherence maps of the co-event period present a dark polygon that is related to incoherent change or deformation. But inside the AoI, the results show some coherent changes which mean that this area has deformed as a block up or down.

`8
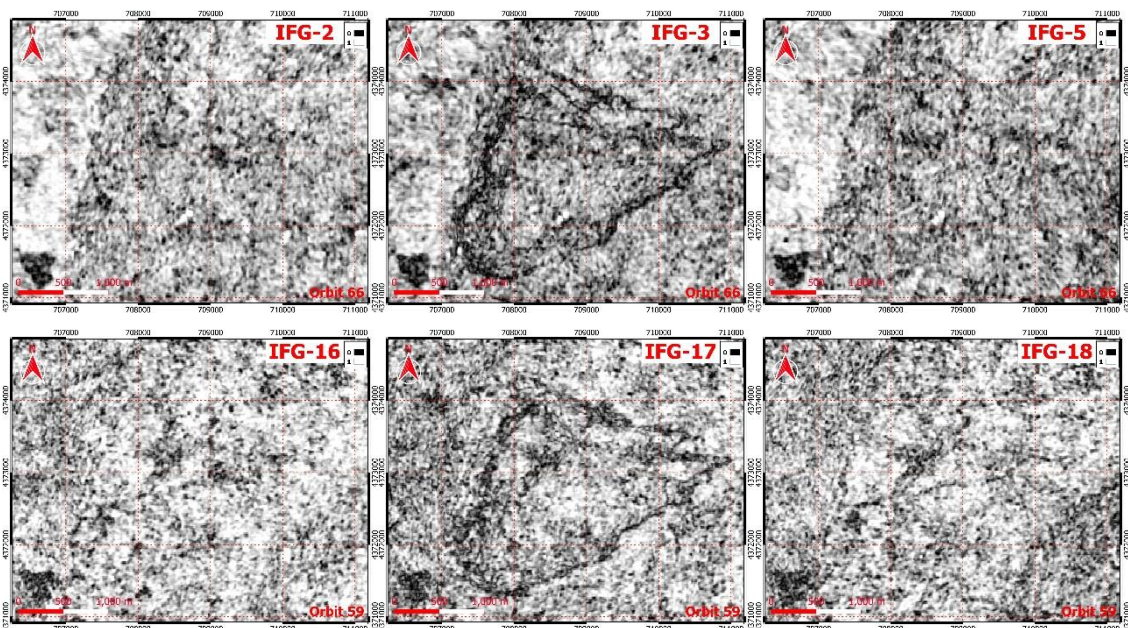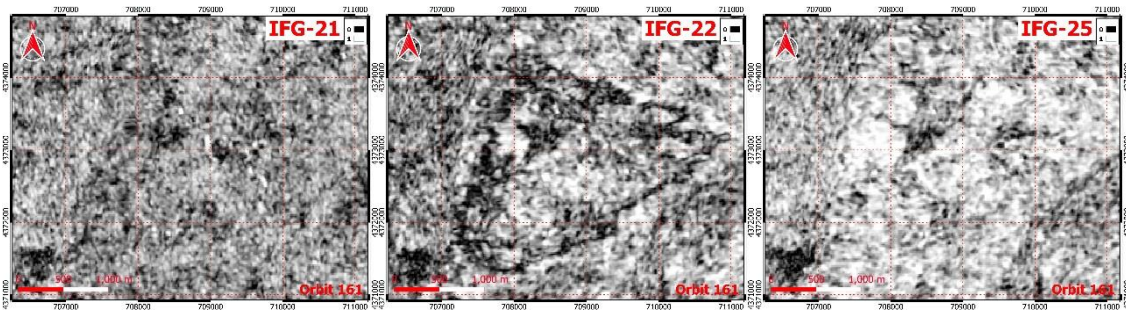
Figure 8. Coherence maps of Grarem AoI: the images represent pre-event (left), co-event (middle), and post-event (right) for orbits 66, 59, and 161. *Nota: the co-event maps for the three orbits show the decay of coherence that is triggered by the earthquake.*

According to phase and coherence maps, the affected area is approximately 3.94 km^2, with an average runout distance of 2.6 km from top to downhill (Fig. 2.a distance from point 1 to point 2).
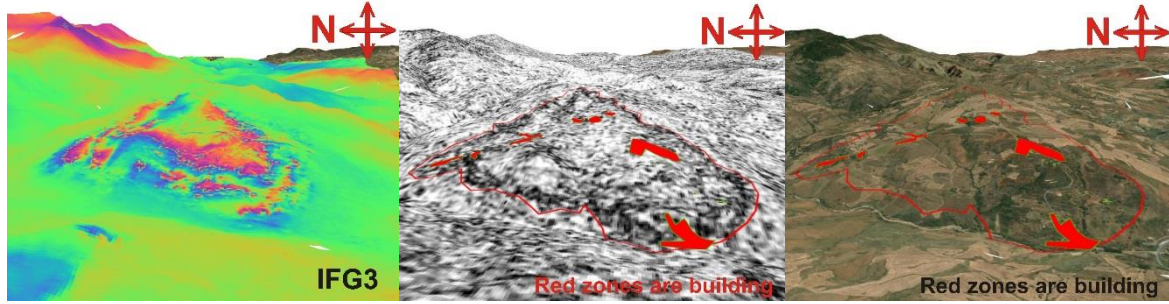
Figure 9. 3D view of Grarem Area, Images of IFG-3. Each fringe = wavelength/2 in LOS, and red zones represent existing building compounds (QGIS, ESRI basemap).

4.2 Case of Kherba

DInSAR has abundantly demonstrated its reliability as a technique for monitoring slow movements (Cascini et al., 2013; Wempen, 2020). In the present study, Kherba's landslides exceed the capabilities of DInSAR since this method cannot measure the deformations due to incoherent change at the first event. Phase images of the Region of Interest (RoI) show a clear decorrelation and consequently, the phase information is no longer convenient for analysis.
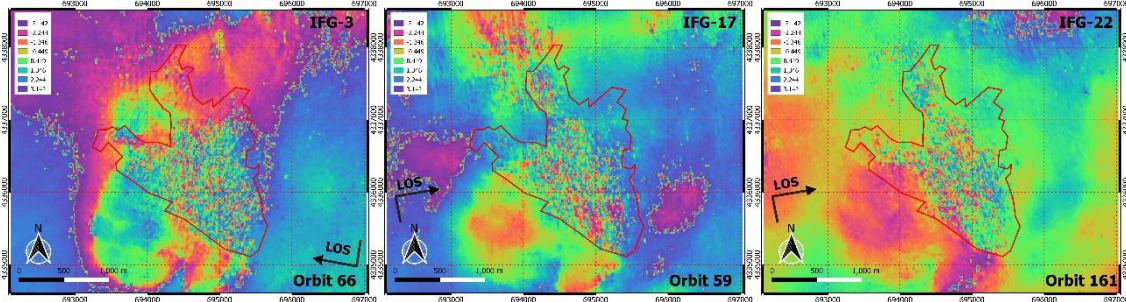
Figure 10. Kherba main event interferograms, biased pixels inside the red line correspond to incoherent changes.

In such cases of incoherent changes in the scene, DInSAR is useless whereas the Coherence Change Detection (CCD) method remains useful and suitable to monitor the event.

4.2.1 CCD Times series analyses

For the case study, the coherence maps (Figs. 11-13) show very low coherence in the Kherba area, indicating that some changes have occurred. The CCD quantifies changes between two SAR images and is represented as a decay of coherence values (co-event maps). Decreases in coherence values can be caused by a variety of factors such as geotechnical landslides as well as water, vegetation. To distinguish between natural low coherence and induced surface changes, a second coherence map (pre-event or post-event) is required to serve as a reference, which can be compared with the main co-event images. It is preferable

239 to mask out the rest of the non-changed area using a pre-event to co-event image ratio and filter values equal to or less than 1
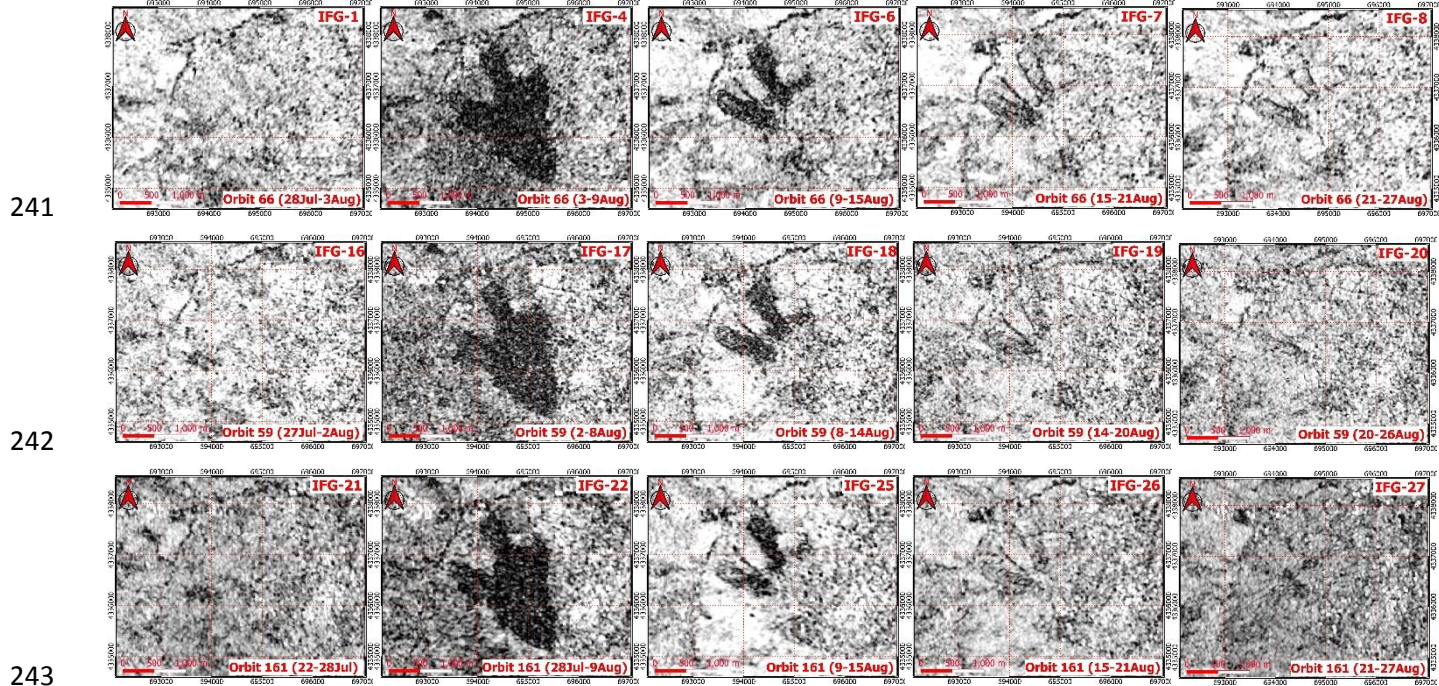
240 (see Fig. 13).

Figure 11. Coherence time series maps of the Kherba landslide, Sentinel-1.
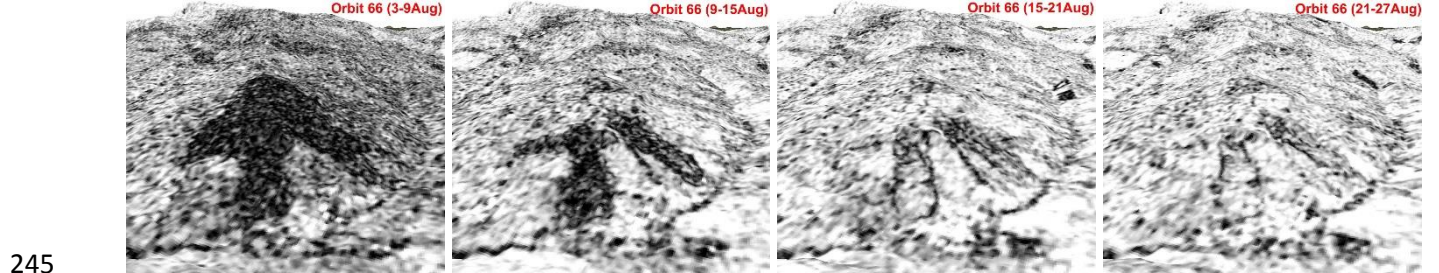
Figure 12. 3D view of Kherba landslide, Sentinel-1 Coherence images of Orbit 66 with a 6-day temporal baseline, the dark areas are the landslide and deformations zones.

The CCD time-series analysis displays the changes in the AoI over time for the Kherba landslide. The dark region represents the main changes that occurred during the co-event period (earthquake date). The landslide shape is divided into two toes at the lower side of the Hill, as shown in Figs. 11 and 12.

During the first week following the earthquake, changes are detected in the lower side of the hill and lasted until the late date of August 2020 (IFG-8 orbits 66, IFG-27 orbit161, and IFG-20 for orbit 59). Afterwards, many other sources of noise were present in the AoI, which makes this technique less efficient (weather, human activities). Most of the processed images are 6 days' intervals, except the orbit 161 in which the co-event interferogram (IFG-24) was not good enough (bad coherence) to compare with other pre-post-event images, so it was replaced by the IFG-22. Figures 14 and 15 illustrate how the interferograms selection may change the interpretation of results.

To quantify the change, an RoI represented in Fig. 13 (green rectangle) is selected for analysis. The plots in Figs. 14 and 15 show also the frequency distributions of coherence values within the RoI. Table 3 displays the calculated average coherence values of the RoI and the percentage of changes. For the orbit 66 pairs, the RoI average coherence starts by 0.66 during the pre-event period (IFG-2) and decreases to 0.51 during the co-event period (-23%) (IFG-3). For orbit 59 pairs, it decreases by 22% after an initial mean value of 0.77 (IFG-16) and a mean value of 0.60 (IFG-17).

262
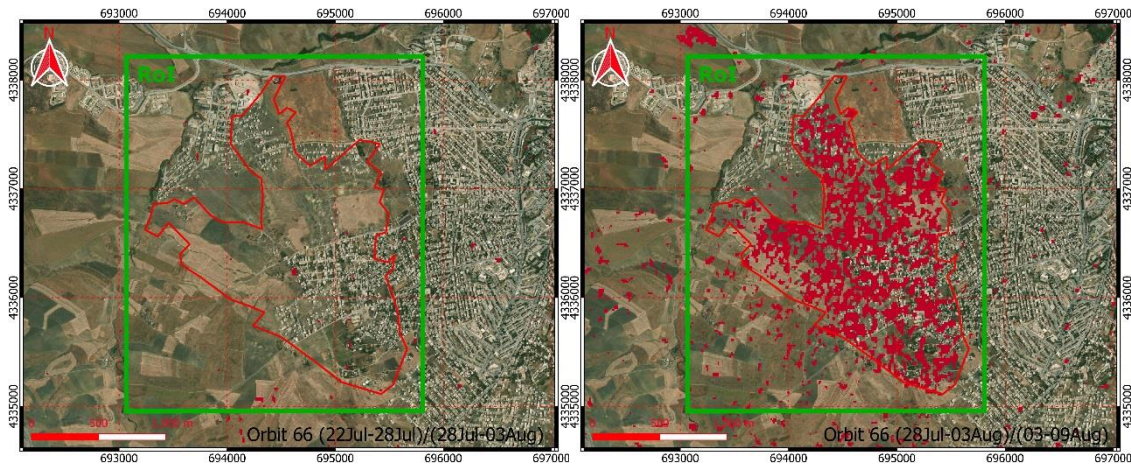
263 **Figure 13.** Pre-event coherences ratio (left), co-event coherences ratio (right), Sentinel-1 Orbit 66. The green box indicates the scope of the
264 RoI, red spots represent significant changes of coherence in the landslide region (QGIS, ESRI World Imagery basemap).

265 The last orbit 161 pairs make an exception due to the initial bad coherence maps (IFG-23 and 24), as shown in Fig. 15, where

266 the dotted green line has low coherence compared to the co-event coherence map (red dotted line). So, the orbit 161 acquisition

267 of the 3rd August must be skipped and not used for the analysis. It was replaced by the previous acquisition on July 28th.

268 However, the previous pair (IFG-21 and IFG-22) had a value of 0.57 (IFG-21) that decreased to 0.52 (IFG-22), representing a

269 9 percent of change.

270 **Table 3.** Mean coherence change values inside the ROI.

Orbit	Pre-event coherence mean	Co-event coherence mean	Post-event coherence mean	Pre-event Change	Post-event Change
66	28Jul_03Aug	03_09Aug	09_15Aug	-23%	+24%
	0.66	0.51	0.63		
59	27Jul_02Aug	02_08Aug	08_14Aug	-22%	+15%
	0.77	0.60	0.69		
161	22Jul_28Jul	28Jul_09Aug	09Aug _15Aug	-9%	+37%
	0.57	0.52	0.71		

271 The lines in Figure 14 indicate the frequency distributions of coherence time series maps. The green line in Fig.14.a represents

272 the pre-event coherence distribution, while the red line represents the post-event coherence distribution, which clearly shows

273 a decay of the mean coherence after the main event (dates and values are presented in the legend).

274
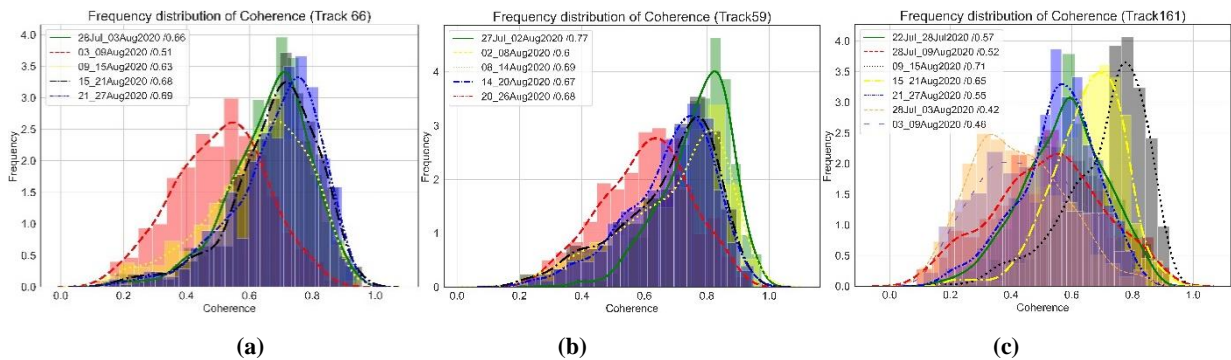
275 **(a)** **(b)** **(c)**
276 **Figure 14.** Frequency distributions of coherence values within RoI for all coherence time series images.

277 Figure 15 illustrates why the interferogram of the 22-28July (green line) is chosen as the pre-event (initial) even though there

278 is another IFG of (28July-3Aug green dotted line) i.e. only four days before the main event (7 August 2020).

279
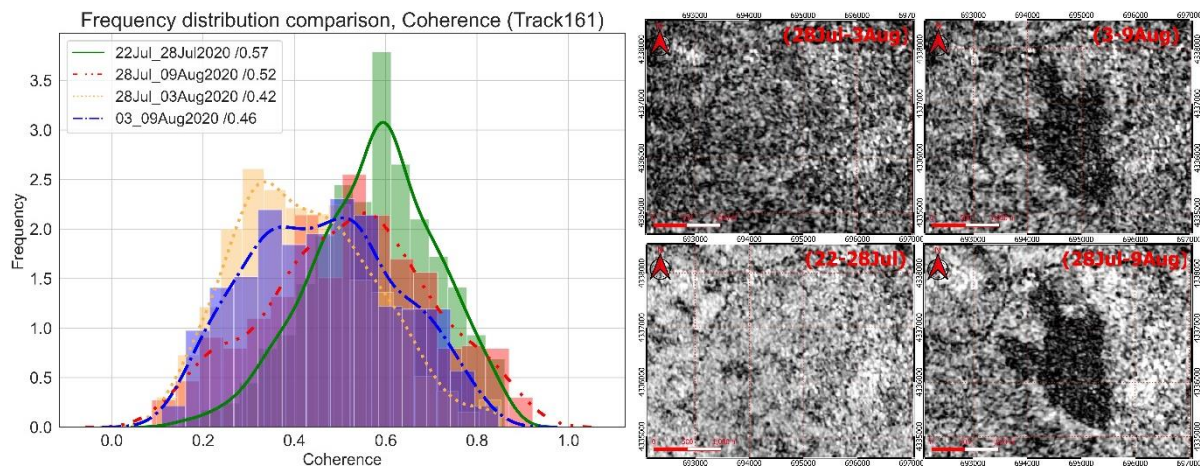
Figure 15. Effect of bad coherence: the cause is the acquisition of 3rd August start at (17:28:15, orbit 161) under bad weather conditions in the acquisition time according to precipitation site (WWO) (rainfall in that daytime), compared to the acquisition of the same day but not the same time (05:37:58 for orbit 66).

The surface area derived from the coherence images covers 2.1 km^2, and the shape ends by two toes. The runout distance is 2.4 km for the right toe and 2.15 km for the left one. The CCD method has the potential to differentiate between the areas impacted by induced changes and those affected by other sources of noise. The ratio operation is useful in canceling out other noise factors and improving the detection of changes in the region.

4.2.2 Optical detection

To validate the SAR methods results, two images from Sentinel-2 are downloaded and treated using QGIS software, the dates of the images are 2020-07-30 (a week before the main shock), and 2020-08-09 (two days after the main shock).

- The optical detection shows that an important displacement affected the ground in the Kherba neighborhood, over an area of 1.32 km^2. The landslide shape of deformation has only one toe at the lower part of the hill (blue line Fig. 16.b) compared to the CCD method results.

(a)   **(b)**
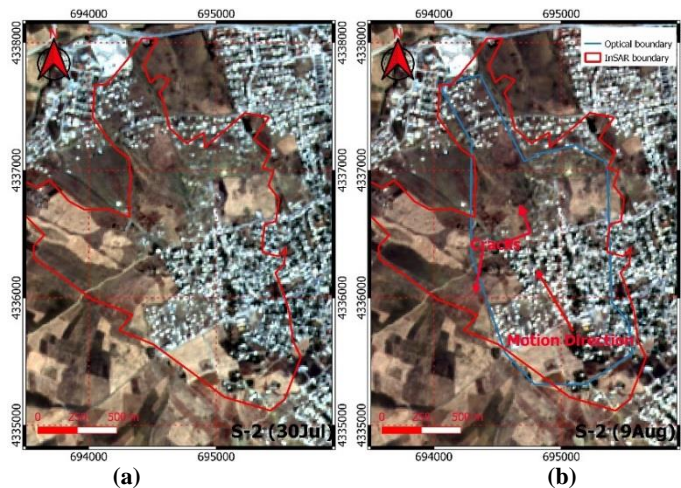
Figure 16. Sentinel-2 Optic Images: (a)- dated 30-Jul 2020, (b)- dated 09-Aug 2020.

- The optical images were unable to detect the ground deformations and displacements in Grarem in which there was no apparent landslide although there were a lot of ruptures and cracks. However, a field inspection has confirmed the results of the CCD and DInSAR analysis in terms of pattern and limits of the zone affected by the deformation (surface rupture).

4.3 LiCSBAS analyses

Displacement time series and velocities analysis of the region is performed out using LiCSBAS that exploits the data of the LiCSAR system (Morishita, 2021). It allows identifying whether unstable conditions pre-existed or are still undergoing. The

study started from the 5th of April to the 26th of September 2020, for the orbit 66 and from 26 April 2015 to 26 September 2020 for the orbit N° 161.
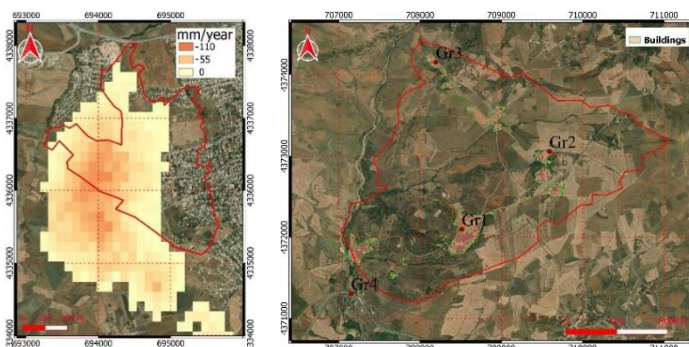
(a)   (b)**Figure 17. (a)** Line of sight displacement velocity map, the red line is landslide area (066D_05394_131311), (b) Grarem case selected points for time-series analysis, (QGIS, ESRI basemap).

The time-series analysis detected subsidence of the west part of Kherba. This region is on the other hillside of Kherba Hill, and both sides have a significant slope. A site investigation did not find any drilled wells. One may assume that this subsidence is not caused by the pumping of groundwater. Therefore, another possible explanation is probably related to the large mass movement of the main landslide hillside (red polygon), causing the opposite side of the hill to move down (subsidence). The displacement velocity in Kherba is about 110 mm/year, Fig. 17.

For the Grarem case, the velocity map looks stable between the same dates (April 5 to September 26, 2020). The change occurred rapidly and is removed by the filters. For illustrative purposes, the displacement time series of some points are illustrated in Figs. 18 and 19.
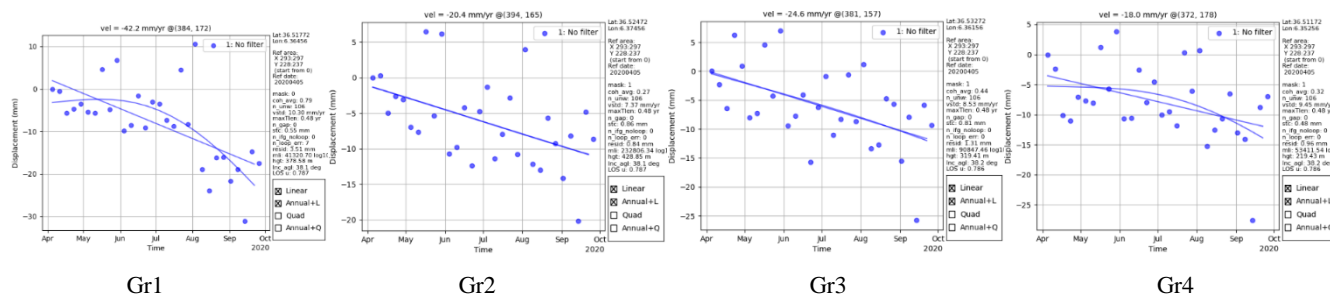
Gr1   Gr2   Gr3   Gr4

Figure 18. Displacement time series (orbit 66, Grarem case), corresponding to the points in image (17.b), the displacement is relative to a reference point, the plots present a great dispersion of data points which is related to many noise resources (weather, man-made, etc.), and short period of analysis, (QGIS, ESRI basemap).

Gr1   Gr2

Gr3   Gr4
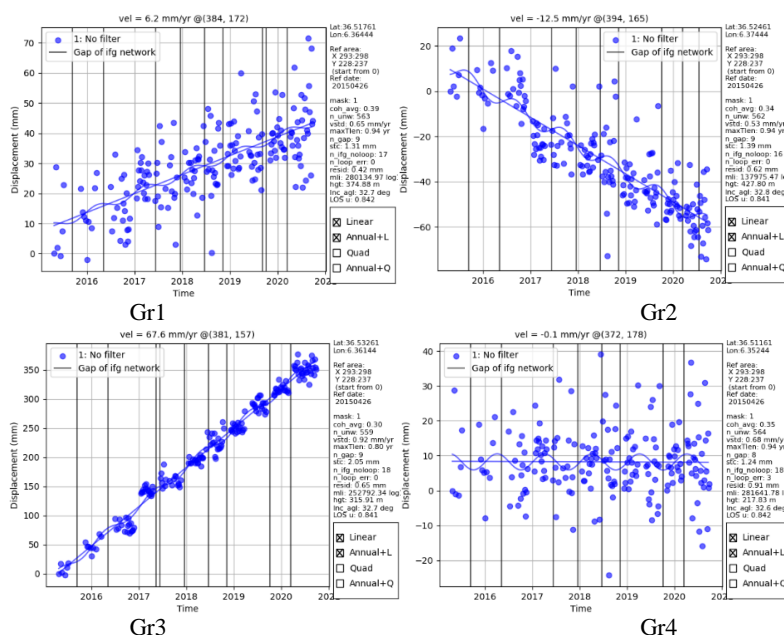
Figure 19. Displacement time series (orbit 161), corresponding to the points in Fig. 17.b, The plots show less dispersion of data points (linear) compared to short analysis, the long period analysis (5 years) is useful to eliminate other sources of noise.

`13

327   During the LiCSBAS processing, a primary stable reference point is selected at (36.455885° N, 6.276909° E). This method
328 proves to be efficient for large-scale deformation monitoring and slow coherent changes, long time series analysis is useful in
329 reducing other noise factors.

4.4 Discussion

331 InSAR monitoring proves its ability to detect land changes. First, landslides and land deformation can be detected remotely by
332 InSAR. Furthermore, optical images could detect only one case (Kherba). The theoretical results were validated by site visiting
333 and investigation, i.e.:

334   - Compared to results obtained from optical for the Kherba landslide, InSAR is more precise for detecting small
335   deformation (2 toes in CCD maps). Besides, the optical analysis did not detect the full deformed area in the region (only
336   one toe).
337   - Large-scale landslides exceed DInSAR's capabilities, which induce an extreme loss of coherence. The co-event
338   interferograms are strongly decorrelated. Therefore, the phase information is no longer usable and one cannot measure
339   the displacement of incoherent ground changes (Landslide).
340   - Land deformation in Grarem first detected by DInSAR, was confirmed by a site visit, during which small cracks were
341   visible on the ground (incoherent boundary region). Due to incoherent boundaries and because the displacement is
342   probably larger than what can be measured by one fringe cycle (depending on the wavelength, 5 cm for Sentinel-1), the
343   deformation measurements in this case are not reliable and accurate.
344   - Another landslide detected by InSAR in the Azeba region (6 km east of Mila) was visited too: the area covers 0.42 km^2
345   and the site investigation confirms the landslide (Fig. 20).
346   - Analysis with LiCSBAS revealed new hillside deformation (subsidence) which is probably a consequence of the mass
347   that moved in the main landslide hillside. Displacements time series, of the Grarem region at some points, show
348   deformation along LOS with velocities ranging from 6 mm/year to 67 mm/year. This method is preferable in large-scale
349   area and long-period analysis.

350
351   **(a)**   **(b)**   **(c)**
352 **Figure 20.** Landslide occurred in Azeba region (2 km North) detected by InSAR: *(a) & (b)- visible ground cracks, (c)- coherence map of*
353 *Azeba zone delimited by the cracks*.

5 Conclusions and Recommendations

355 In this paper, active and passive space-based satellite data are used to monitor and study the impact of natural hazards
356 (earthquakes and landslides) on struck areas. The C-band Sentinel-1 SAR datasets (active sensing) and optical images of
357 Sentinel-2 data (10 m spatial resolution) were used in this study to investigate the area, the passive images were used only to
358 validate the active sensing results. For the InSAR processing, the use of DInSAR, CCD methods, and the LiCSBAS tools have
359 been able to generate a detailed time series analysis of ground changes.
360 InSAR techniques have proved their efficiency to extract useful geodetic information, such as the ground movement and track
361 surface deformation over large areas with centimetric accuracy in coherent change cases. The present research study has

demonstrated that the InSAR processing is adapted to study earthquake and landslides zones. As a result, three primary land failures were detected over the study area using InSAR.

DInSAR is poorly suited to track and detect landslides. It is represented as a pixel decorrelation in phase interferograms and high decay in coherence values. CCD is further suitable to map earthquake-induced landslides that may remain undetected using coherent methods (DInSAR). The estimation of their horizontal/vertical displacements is a challenge to be inferred.

The Grarem deformation looks like a landslide that has just been initiated but might extend under an upcoming triggering event. Actually, the failure plane rim is presented as a dark line in the coherence map or as the fringe circumference in phase maps (estimated area 3.94 sq. km). This impending land failure needs therefore a thorough and real-time monitoring by the PS-InSAR method, which can provide efficient and low-cost monitoring method able to obtain millimeter-level precision displacement measurements over selected points in the area (Jia et al., 2019), and adequate geotechnical studies.

It is worth increasing awareness of possible future geotechnical threats in a timely manner, through on-site monitoring using GPS, crack meters, and by placing inclinometers in the Grarem area, in order to develop a model of the slope stability.

Acknowledgments: In this work, we used SNAP and QGIS to analyze and plot maps. The authors are grateful to European Space Agency (ESA) for providing freely the data through Copernicus Program and COMET.

Conflicts of Interest: The authors declare no conflict of interest.

References

ASF DAAC: Alaska Satellite Facility, [online] Available from: https://search.asf.alaska.edu/#/ (Accessed 26 June 2021), n.d.

Bakon, M., Perissin, D., Lazecky, M. and Papco, J.: Infrastructure Non-linear Deformation Monitoring Via Satellite Radar Interferometry, Procedia Technol., 16, 294–300, doi:10.1016/j.protcy.2014.10.095, 2014.

Braun, A.: Radar satellite imagery for humanitarian response: Bridging the gap between technology and application, , 225 [online] Available from: https://publikationen.uni-tuebingen.de/xmlui/bitstream/handle/10900/91317/Braun 2019 Radar satellite imagery for humanitarian response UB.pdf?sequence=1, 2019.

Canaslan Çomut, F., Gürboğa, Ş. and Smail, T.: Estimation of co-seismic land deformation due to Mw 7.3 2017 earthquake in Iran (12 November 2017) using Sentinel-1 DInSAR, Bull. Miner. Res. Explor., 162(August), 11–30, doi:10.19111/bulletinofmre.604026, 2020.

Cascini, L., Peduto, D., Pisciotta, G., Arena, L., Ferlisi, S. and Fornaro, G.: The combination of DInSAR and facility damage data for the updating of slow-moving landslide inventory maps at medium scale, Nat. Hazards Earth Syst. Sci., 13(6), 1527–1549, doi:10.5194/nhess-13-1527-2013, 2013.

Congedo, L.: Semi-Automatic Classification Plugin: A Python tool for the download and processing of remote sensing images in QGIS, J. Open Source Softw., 6(64), 3172, doi:10.21105/joss.03172, 2021.

ESA: ESA's radar observatory mission for GMES operational services. [online] Available from: https://sentinel.esa.int/documents/247904/349449/S1_SP-1322_1.pdf, 2012.

ESA: Resolution and Swath - Sentinel-1 - Missions - Sentinel Online - Sentinel, [online] Available from: https://sentinel.esa.int/web/sentinel/missions/sentinel-1/instrument-payload/resolution-swath (Accessed 26 June 2021a), n.d.

ESA: SAR Instrument - Sentinel-1 SAR Technical Guide - Sentinel Online - Sentinel, [online] Available from: https://sentinels.copernicus.eu/web/sentinel/technical-guides/sentinel-1-sar/sar-instrument (Accessed 26 June 2021b), n.d.

Frizon de Lamotte, D., de Lamotte, D. F., Bezar, B. Saint, Bracène, R. and Mercier, E.: The two main steps of the Atlas building and geodynamics of the western Mediterranean, Tectonics, 19(4), 740–761 [online] Available from: https://www.academia.edu/29649745/The_two_main_steps_of_the_Atlas_building_and_geodynamics_of_the_western_Mediterranean (Accessed 6 January 2022), 2000.

Galve, J. P., Castañeda, C. and Gutiérrez, F.: Railway deformation detected by DInSAR over active sinkholes in the Ebro Valley evaporite karst, Spain, Nat. Hazards Earth Syst. Sci., 15(11), 2439–2448, doi:10.5194/nhess-15-2439-2015, 2015.

Goudarzi, M. a: Detection and measurement of land deformations caused by seismic events using InSAR, Sub-pixel correlation, and Inversion techniques, , (January), 127, 2010.

Herrera, G., Fernández, J. A., Tomás, R., Cooksley, G. and Mulas, J.: Advanced interpretation of subsidence in Murcia (SE Spain) using A-DInSAR data - Modelling and validation, Nat. Hazards Earth Syst. Sci., 9(3), 647–661, doi:10.5194/nhess-9-647-2009, 2009.

Hooper, A., Zebker, H., Segall, P. and Kampes, B.: A new method for measuring deformation on volcanoes and other natural terrains using InSAR persistent scatterers, Geophys. Res. Lett., 31(23), 1–5, doi:10.1029/2004GL021737, 2004.

Jacquemart, M. and Tiampo, K.: Leveraging time series analysis of radar coherence and normalized difference vegetation index ratios to characterize pre-failure activity of the Mud Creek landslide, California, Nat. Hazards Earth Syst. Sci., 21(2), 629–642, doi:10.5194/nhess-21-629-2021, 2021.

Jia, H., Zhang, H., Liu, L. and Liu, G.: Landslide deformation monitoring by adaptive distributed scatterer interferometric synthetic aperture radar, Remote Sens., 11(19), 1–18, doi:10.3390/rs11192273, 2019.

Jung, J. and Yun, S. H.: Evaluation of coherent and incoherent landslide detection methods based on synthetic aperture radar for rapid response: A case study for the 2018 Hokkaido landslides, Remote Sens., 12(2), 1–26, doi:10.3390/rs12020265, 2020.

Kim, J. W.: Applications of Synthetic Aperture Radar (SAR)/ SAR Interferometry (InSAR) for Monitoring of Wetland Water Level and Land Subsidence, Ohio State Univ., (503), 1–111, 2013.

Laneve, G., Bruno, M., Mukherjee, A., Messineo, V., Giuseppetti, R., De Pace, R., Magurano, F. and Ugo, E. D. ’: Remote Sensing Detection of Algal Blooms in a Lake Impacted by Petroleum Hydrocarbons, Remote Sens. 2022, Vol. 14, Page 121, 14(1), 121, doi:10.3390/RS14010121, 2021.

Lazeckỳ, M., Hatton, E., González, P. J., Hlaváčová, I., Jiránková, E., Dvořák, F., Šustr, Z. and Martinovič, J.: Displacements monitoring over Czechia by IT4S1 system for automatised interferometric measurements using Sentinel-1 data, Remote Sens., 12(18), 1–21, doi:10.3390/RS12182960, 2020a.

Lazeckỳ, M., Spaans, K., González, P. J., Maghsoudi, Y., Morishita, Y., Albino, F., Elliott, J., Greenall, N., Hatton, E., Hooper, A., Juncu, D., McDougall, A., Walters, R. J., Watson, C. S., Weiss, J. R. and Wright, T. J.: LiCSAR: An automatic InSAR tool for measuring and monitoring tectonic and volcanic activity, Remote Sens., 12(15), doi:10.3390/RS12152430, 2020b.

LNHC: Laboratoire National de l'Habitat et de la Construction, LNHC [online] Available from: http://lnhc-dz.com/ (Accessed 26 June 2021), n.d.

Mazzanti, P., Rocca, A., Bozzano, F., Cossu, R. and Floris, M.: Landslides Forecasting Analysis By Displacement Time Series Derived From Satellite INSAR Data: Preliminary Results, undefined, 2012.

Meng, Q., Confuorto, P., Peng, Y., Raspini, F., Bianchini, S., Han, S., Liu, H. and Casagli, N.: Regional recognition and classification of active loess landslides using two-dimensional deformation derived from sentinel-1 interferometric radar data, Remote Sens., 12(10), doi:10.3390/rs12101541, 2020.

Merghadi, A., Abderrahmane, B. and Tien Bui, D.: Landslide susceptibility assessment at Mila basin (Algeria): A comparative assessment of prediction capability of advanced machine learning methods, ISPRS Int. J. Geo-Information, 7(7), doi:10.3390/ijgi7070268, 2018.

Moretto, S., Bozzano, F. and Mazzanti, P.: The role of satellite insar for landslide forecasting: Limitations and openings, Remote Sens., 13(18), 1–31, doi:10.3390/rs13183735, 2021.

Morishita, Y.: Nationwide urban ground deformation monitoring in Japan using Sentinel-1 LiCSAR products and LiCSBAS, Prog. Earth Planet. Sci., 8(1), doi:10.1186/s40645-020-00402-7, 2021.

445 Mouloud, H. and Badreddine, S.: Probabilistic seismic hazard assessment in the Constantine region, Northeast of Algeria,
446 Arab. J. Geosci., 10(6), doi:10.1007/s12517-017-2876-5, 2017.

447 Netzband, M., Stefanov, W. L. and Redman, C.: Applied remote sensing for urban planning, governance and sustainability.,
448 2007.

449 Pawluszek-Filipiak, K. and Borkowski, A.: Integration of DInSAR and SBAS techniques to determine mining-related
450 deformations using Sentinel-1 data: The case study of rydultowy mine in Poland, Remote Sens., 12(2),
451 doi:10.3390/rs12020242, 2020.

452 Peláez Montilla, J. A., Hamdache, M. and Casado, C. L.: Seismic hazard in Northern Algeria using spatially smoothed
453 seismicity. Results for peak ground acceleration, Tectonophysics, 372(1–2), 105–119, doi:10.1016/S0040-1951(03)00234-8,
454 2003.

455 Rapant, P., Struhár, J. and Lazeckỳ, M.: Radar interferometry as a comprehensive tool for monitoring the fault activity in the
456 vicinity of underground gas storage facilities, Remote Sens., 12(2), doi:10.3390/rs12020271, 2020.

457 Roque, D., Perissin, D., Falcão, A. P., Fonseca, A. M. and Maria, J.: Dams regional safety warning using time-series insar
458 techniques, Second Internatinal Dam World Conf., 21–24, 2015.

459 Sanabria, M. P., Guardiola-Albert, C., Tomás, R., Herrera, G., Prieto, A., Sánchez, H. and Tessitore, S.: Subsidence activity
460 maps derived from DInSAR data: Orihuela case study, Nat. Hazards Earth Syst. Sci., 14(5), 1341–1360, doi:10.5194/nhess-
461 14-1341-2014, 2014.

462 Tampuu, T., Praks, J., Uiboupin, R. and Kull, A.: Long term interferometric temporal coherence and DInSAR phase in
463 Northern Peatlands, Remote Sens., 12(10), 7–9, doi:10.3390/rs12101566, 2020.

464 Tzouvaras, M., Danezis, C. and Hadjimitsis, D. G.: Small scale landslide detection using Sentinel-1 interferometric SAR
465 coherence, Remote Sens., 12(10), doi:10.3390/rs12101560, 2020.

466 USGS: M 5.0 - 3 km NNE of Sidi Mérouane, Algeria, [online] Available from:
467 https://earthquake.usgs.gov/earthquakes/eventpage/us6000bag6/executive (Accessed 26 June 2021a), n.d.

468 USGS: USGS Earthquake Hazards Program, [online] Available from: https://earthquake.usgs.gov/ (Accessed 26 June
469 2021b), n.d.

470 Wang, Z., Li, Z. and Mills, J.: A new approach to selecting coherent pixels for ground-based SAR deformation monitoring,
471 ISPRS J. Photogramm. Remote Sens., 144, 412–422, doi:10.1016/j.isprsjprs.2018.08.008, 2018.

472 Wempen, J. M.: International Journal of Mining Science and Technology Application of DInSAR for short period
473 monitoring of initial subsidence due to longwall mining in the mountain west United States, Int. J. Min. Sci. Technol., 30(1),
474 33–37, doi:10.1016/j.ijmst.2019.12.011, 2020.

475 WWO: Mila, Mila, Algeria Historical Weather Almanac, [online] Available from:
476 https://www.worldweatheronline.com/mila-weather-history/mila/dz.aspx / (Accessed 26 June 2021), n.d.

477